



Ss. Cyril and Methodius University in Skopje



FACULTY OF  
MECHANICAL  
ENGINEERING

# Case Study

# Flow around an airfoil with Ansys Fluent

Marija Lazarevikj, Valentino Stojkovski and Zoran Markov

Edited and curated by the Ansys Academic Development Team

[education@ansys.com](mailto:education@ansys.com)

## Summary

This case study deals with air flow around a NACA 4-digit cambered airfoil. The main aim is to analyze the aerodynamic characteristics i.e., lift coefficient and drag coefficient at different angles of attack and to capture physical phenomena. Validation of the numerical model is obtained by comparison with available experimental data. All phases of CFD analysis are conducted in Ansys Workbench.

## Table of Contents

1. Introduction.....	3
1.1 Airfoil .....	3
1.2 Description of the problem .....	4
2. Setting up the problem in Ansys Workbench .....	4
2. 1 Preprocessing .....	4
2.1.1 Defining the fluid domain .....	4
2.1.2 Meshing.....	5
2.2 Processing.....	5
2.2.1 Choice of turbulence model .....	6
2.2.2 Validation of numerical model .....	6
2.3 Post-processing.....	7
2.3.1 Velocity distribution .....	7
2.3.1.1 Positive angle of attack.....	7
2.3.1.2 Negative angle of attack .....	8
2.3.1.3 Flow field adaptation in front of and behind the airfoil .....	10
2.3.2 Pressure distribution .....	12
2.3.3 Aerodynamic characteristics .....	13
2.3.3.1 lift coefficient $C_l$ .....	14
2.3.3.2 drag coefficient $C_d$ .....	15
3. Conclusions .....	15
4. References .....	16

## 1. Introduction

### 1.1 Airfoil

Airfoils are solid bodies manufactured in such a way that air flowing around them produces useful motion, Figure 1. Examples of airfoils are aircraft wing, turbine blade, propeller blade etc. When set in a velocity field, airfoils are subjected to pressure and viscous forces. The aerodynamic force  $R$  acting on an airfoil consists of two components – a lift force  $L$  directed upwards and acting perpendicular to the free stream direction and a drag force  $D$  acting parallel to the free stream direction, tending to resist the object motion [1] [2].

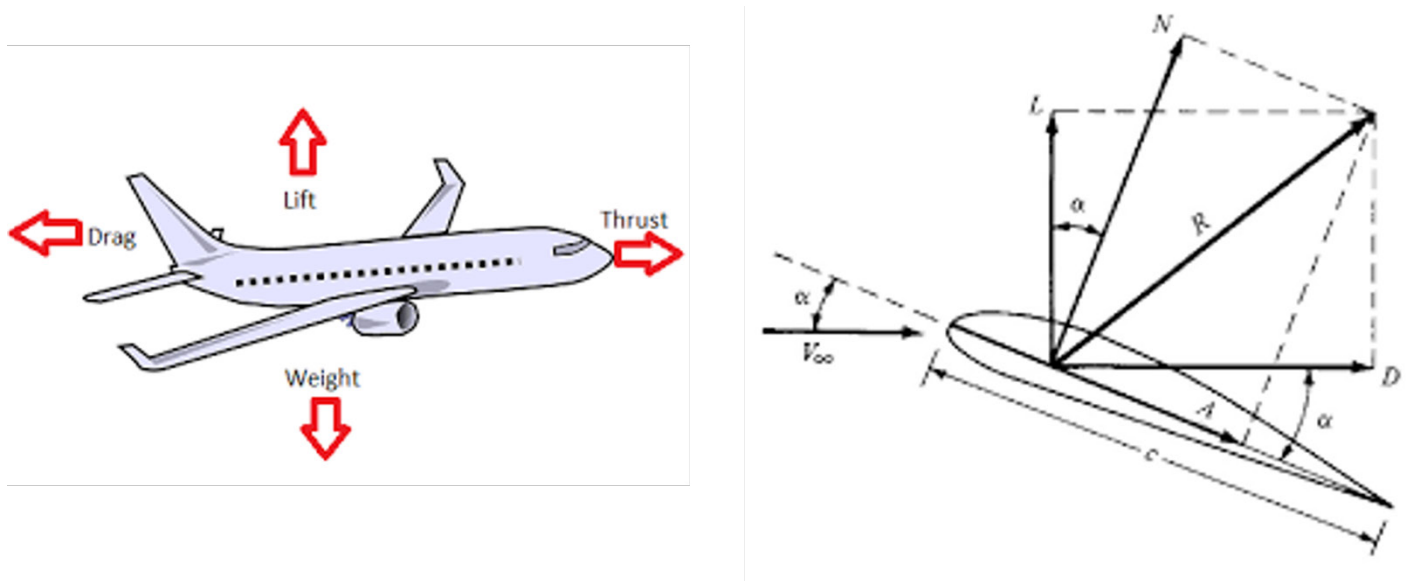


Figure 1 : Aerodynamic forces

The lift and drag force at a certain angle of attack  $\alpha$  can be calculated as:

$$\begin{aligned}L &= N \cos \alpha - A \sin \alpha \\D &= N \sin \alpha + A \cos \alpha\end{aligned}$$

where  $N$  is the normal force acting perpendicular to the chord line, and  $A$  is the axial force acting parallel to the chord line (Figure 1 right).

The airfoil aerodynamic performance is higher if the drag force is small compared to the lift force, i.e., if the airfoil has higher lift to drag ratio  $L/D$ . The determination of aerodynamic forces depends on the flow field characteristics such as velocity, pressure, temperature and density which can be experimentally measured or numerically obtained [3].

The airfoil is defined by the upper and lower contour that enclose a surface and are formed by superposition of thickness distribution, symmetrically around the  $x$ -axis, on a camber line. If the upper and lower contour are symmetrical around the camber line, the airfoil is symmetric, otherwise it is cambered. The chord line connects the leading and trailing edge of the airfoil [4]. The airfoil geometric parameters are shown in Figure 2. The National Advisory Committee for Aeronautics (NACA) has developed standard airfoil shapes for aircraft wings which can be described by analytical expressions. The first family of NACA airfoils is the four-digit series with the first digit defining the maximum camber as percentage of chord, the second digit defining the distance between maximum camber and airfoil

leading edge in tenths of chord and last two digits defining the maximum thickness as percentage of the chord [5].

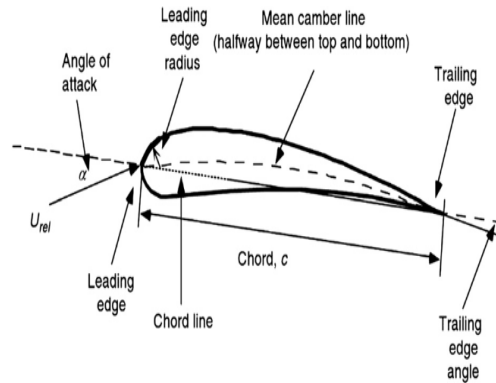


Figure 2 : Airfoil nomenclature

## 1.2 Description of the problem

The aerodynamic characteristics of NACA 4412 airfoil are numerically investigated using Ansys Workbench software. The geometry of the airfoil is given in Figure 3 NACA 4412 is a cambered airfoil with maximum camber at 4% of the chord and its position is at 40% of the chord length, while the airfoil thickness is at 12% of the chord line. The airfoil chord length is  $c=1\text{m}$ . The advantages of a cambered airfoil are lift maximization and minimal stall velocity compared to symmetrical airfoil with similar wing loading.

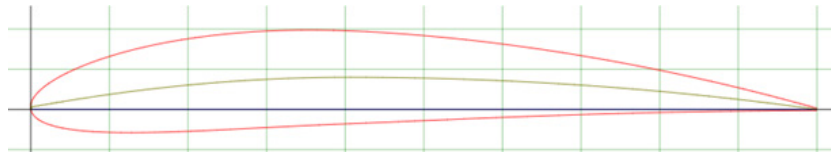


Figure 3 : NACA 4412 geometry [6]

Available experimental data on NACA 4412 aerodynamic characteristics at Reynolds number of  $9 \cdot 10^5$  are found in Report no. 613 by R. M. Pinkerton [7].

Physical properties of air that are considered are constant density  $\rho=1,225 \text{ kg/m}^3$  and dynamic viscosity  $=1,7894 \cdot 10^{-5} \text{ kg/m-s}$ .

The Reynolds number is the ratio between inertial and viscous forces and for airfoil is defined as:

$$Re = \frac{v \cdot c \cdot \rho}{\mu}$$

Thus, the freestream velocity  $v$  is calculated as  $v = \frac{Re \cdot \mu}{c \cdot \rho} = 13,15 \text{ m/s}$ .

## 2. Setting up the problem in Ansys Workbench

### 2.1 Preprocessing

#### 2.1.1 Defining the fluid domain

The NACA 4-digit airfoil generator [6] is used to obtain the airfoil coordinates. Two-dimensional (2D)

flow domain is defined in SpaceClaim<sup>1</sup>, Figure 4. Sufficiently long domain around the airfoil is chosen to minimize influence of fluid disturbance on the leading edge (distance of 5 times the chord length) and to avoid effects of the outlet boundary condition (distance of 20 times the chord length).

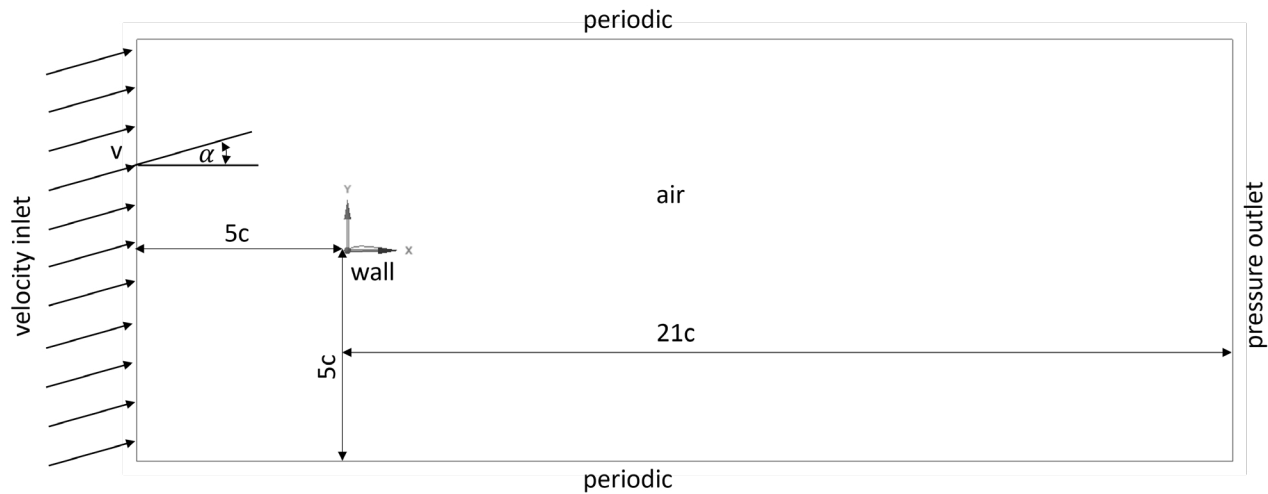


Figure 4 : Flow Domain

### 2.1.2 Meshing

The mesh type and density influence the convergence of the solution and the accuracy of results. By decomposing the computational domain, a fully structured grid is generated with 112710 nodes, Figure 5 left. Considering the importance of proper mesh size near the wall to accurately capture the viscous sublayer, finer mesh is generated around the airfoil (Figure 5 right) following the criteria of keeping the  $y^+$  value beyond 1. Around the airfoil, an O-type grid is generated. Bias option was used in Ansys Meshing. Far away from the airfoil, where large velocity gradients are not expected, the mesh is less dense.

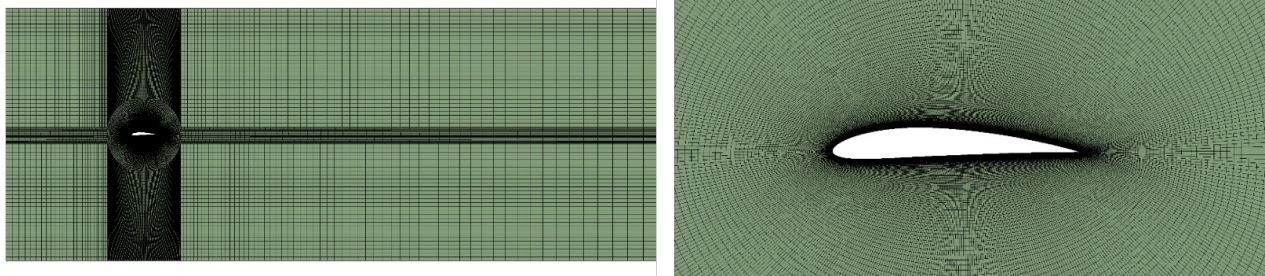


Figure 5 : Mesh of the whole flow domain (left) and finer mesh around the airfoil (right)

After generating the mesh, the boundary surfaces are named as inlet, outlet, airfoil, top and bottom.

## 2.2 Processing

2D viscous and incompressible steady flow of air is modeled and simulated in the Ansys solver Fluent. The boundary condition far upstream of the airfoil is velocity inlet. The calculated velocity 13.15m/s which corresponds to Reynolds number of  $9 \cdot 10^5$  is specified at the inlet boundary using the velocity

<sup>1</sup> After the 2023R1 release, Ansys SpaceClaim became a legacy product and Ansys Discovery (a simulation-driven design tool that combines instant physics simulation, high fidelity simulation and interactive geometry modeling in a single easy-to-use experience) became the primary built-in Geometry tool. If you want to learn more about specifically modeling in Ansys Discovery, check out this Ansys Innovation Course [“Learn Solid Modeling with Ansys Discovery”](#).

magnitude and direction method. The outlet is set to atmospheric pressure. The airfoil walls are set to a no-slip wall condition. The top and bottom of the domain are periodic boundary conditions to simulate an infinite freestream.

Numerical simulations are performed for angles of attack in the range of  $-20^\circ$  to  $+30^\circ$ . The angle of attack is captured by setting the velocity direction.

### 2.2.1 Choice of turbulence model

The Spalart-Allmaras model is chosen for turbulence simulation. It is a one-equation model mainly designed for aerodynamic and turbomachinery applications giving satisfactory results especially for airfoil and turbine blade for which is calibrated. The Spalart-Allmaras model has been validated for external flows and provides good agreement with experimental results in aerospace applications. It is useful for boundary layer flows with arbitrary pressure gradients. Solving a single governing equation to describe viscous flow, the model allows simpler resolution of the eddy viscosity near the wall thus needing lower computational effort [8].

Turbulent-viscosity ratio was set to one. The strain-vorticity based model was selected. The solver is pressure based with absolute velocity formulation.

### 2.2.2 Validation of numerical model

CFD results of the variation of coefficient of pressure along the airfoil for angles of attack, and are compared to experimental results [7], Figure 6.

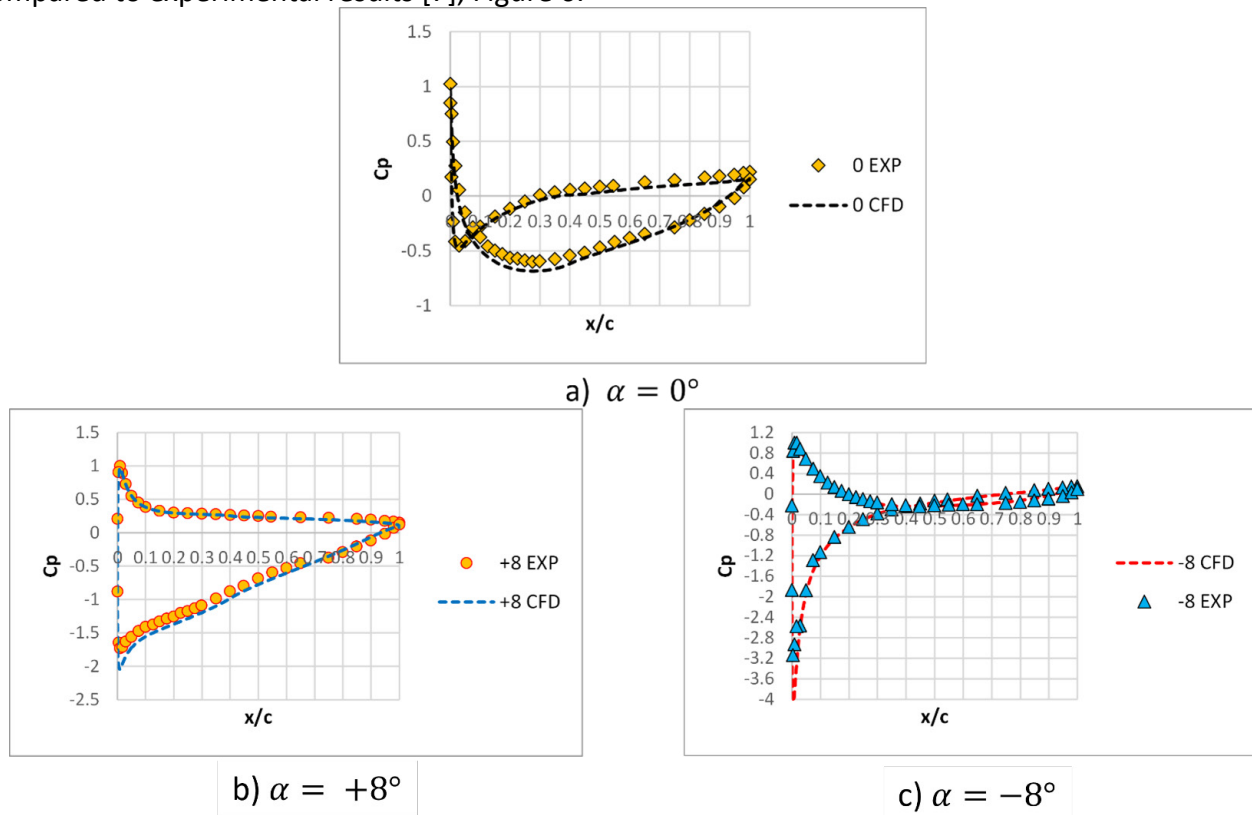


Figure 6 : Comparison between CFD and experimental results for pressure coefficient at different angles of attack



The comparison shows good alignment between the numerically obtained results and the experimental data. The pressure coefficient distribution along the top and bottom surface of the airfoil is fully described by the CFD calculations.

## 2.3 Post-processing

### 2.3.1 Velocity distribution

Velocity vectors show the flow field around the airfoil at different angles of attack. Even at zero angle of attack (Figure 7a), velocity is higher over the upper surface than the bottom surface due to the cambered shape of the airfoil. This means lift is generated at zero angle of attack because there is a pressure difference between the upper and bottom surface. In this case, the leading edge is the stagnation point since it's the location where the air velocity is zero.

Airfoil position in the flow field affects the velocity vectors distribution over the airfoil thus influencing the aerodynamic parameters.

#### 2.3.1.1 Positive angle of attack

In case of positive angle of attack ( $+8^\circ$ ,  $+12^\circ$ , Figure 7b and 7c), the flow conditions around the airfoil leading edge are such that the stagnation point moves further away from the leading edge on the bottom surface. By increasing the angle of attack in a positive direction, the air accelerates at the upper surface, while air at the bottom surface has lower velocity. Moreover, at higher angle of attack ( $+16^\circ$ , Figure 7d), the velocity on the upper surface is higher closer to the leading edge.

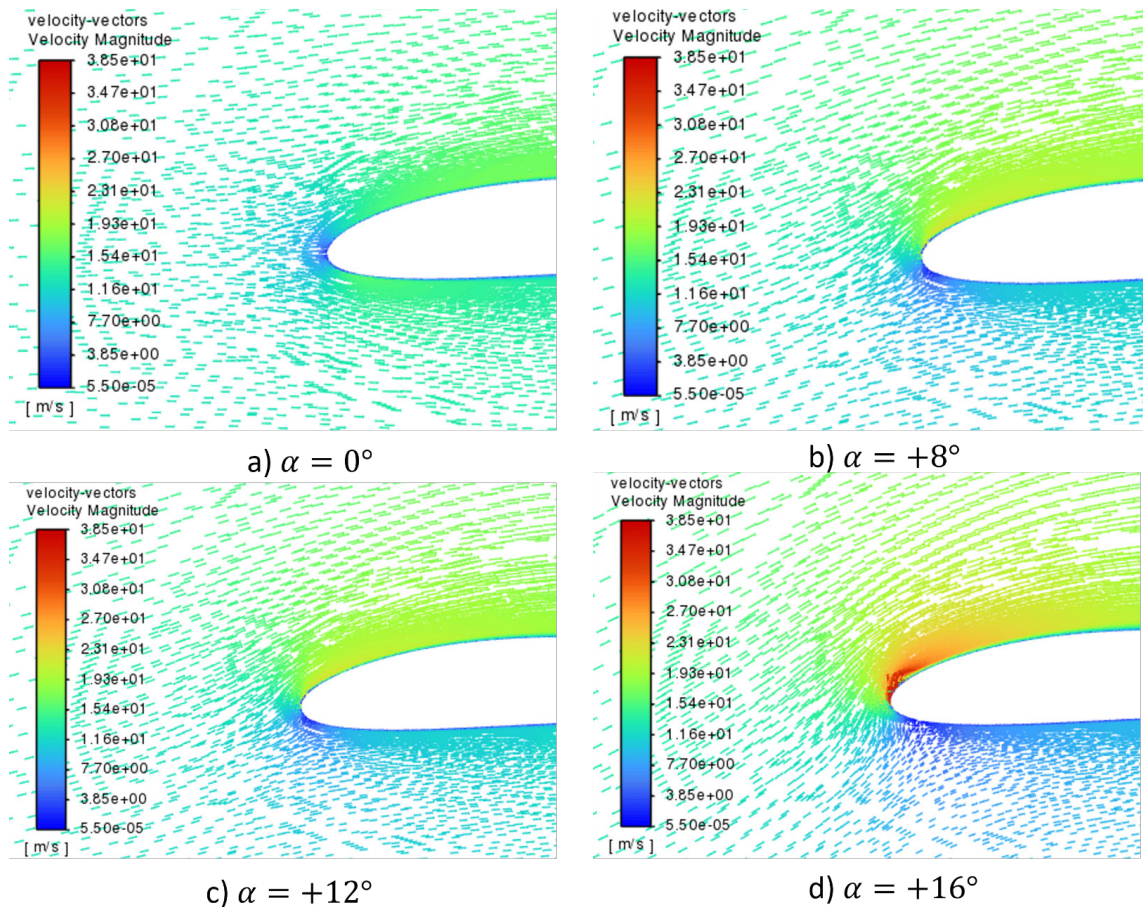


Figure 7 : Influence of a positive angle of attack on the stagnation point location and the velocity distribution around

In case of positive angle of attack, the flow conditions around the airfoil trailing edge change. At larger positive angles of attack ( $+12^\circ$ ,  $+16^\circ$ ,  $+20^\circ$ , Figure 8b, Figure 8c and Figure 8d), the flow tends to separate from the airfoil top surface due to viscous effects. As the angle of attack increases, the separation point moves from the trailing edge towards the leading edge. At  $\alpha = +16^\circ$  (Figure 8c), the flow starts separating closer to trailing edge, on the upper surface. At  $\alpha = +20^\circ$  (Figure 8d), the flow is separated around the middle of the upper surface. A large wake of dead air is created behind the airfoil; the flow in this region is recirculating and part of it is reversed – moving in the opposite direction from the freestream.

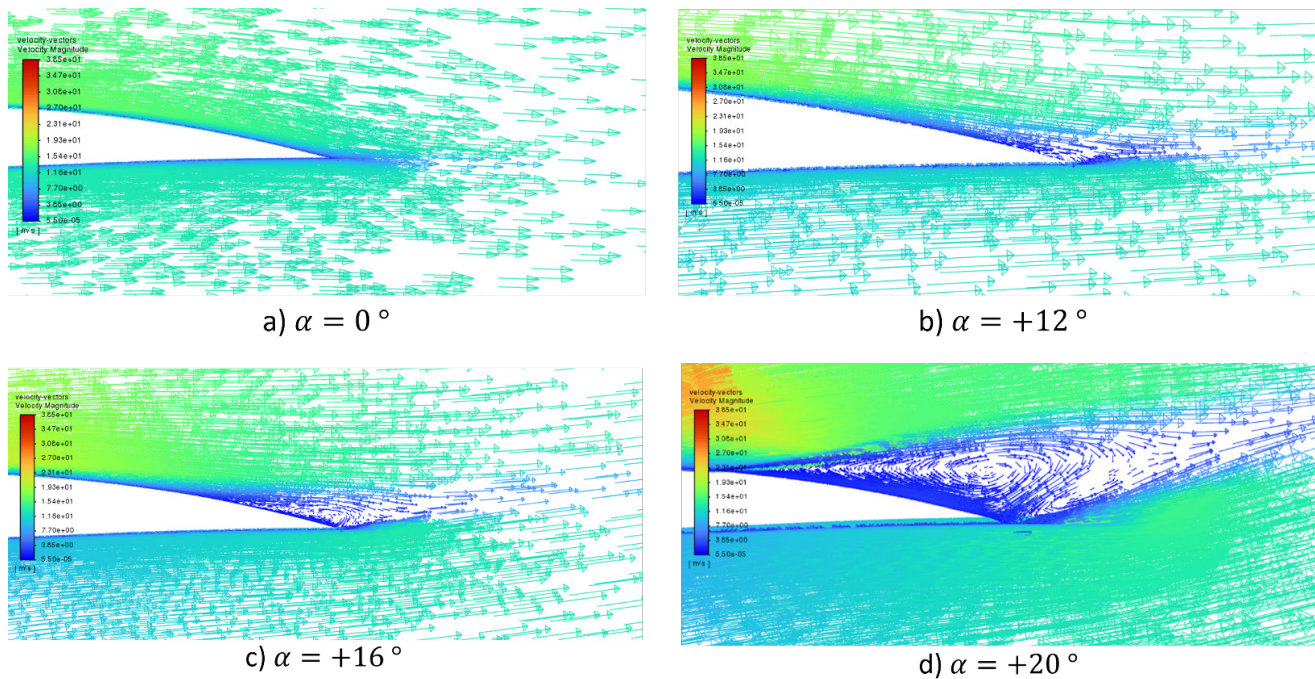


Figure 8 : Influence of a positive angle of attack on the stagnation point location and the velocity distribution around the airfoil trailing edge

### 2.3.1.2 Negative angle of attack

In case of negative angle of attack, the flow conditions around the airfoil leading edge are such that by increasing the angle of attack in negative direction (Figure 9), the stagnation point slowly moves away from the leading edge on the upper surface.



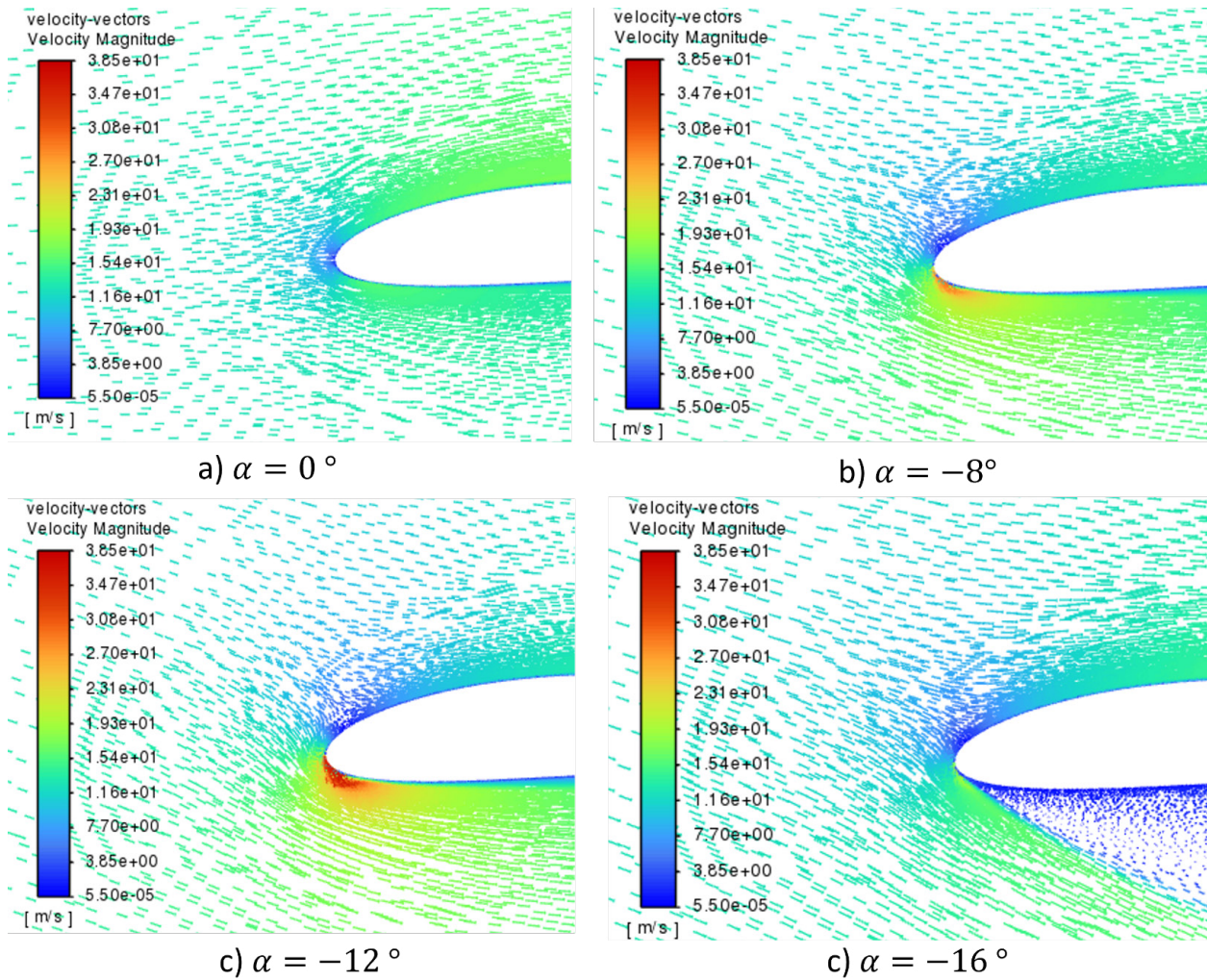


Figure 9 : Influence of a negative angle of attack on the stagnation point location and the velocity distribution around the airfoil leading edge

In case of negative angle of attack, the flow conditions around the airfoil trailing edge change. For  $\alpha = -12^\circ$  (Figure 10c), the separation point is very close to the trailing edge. For  $\alpha = -16^\circ$  (Figure 10d) the flow is already fully separated on the bottom surface with the separation point close to the leading edge.

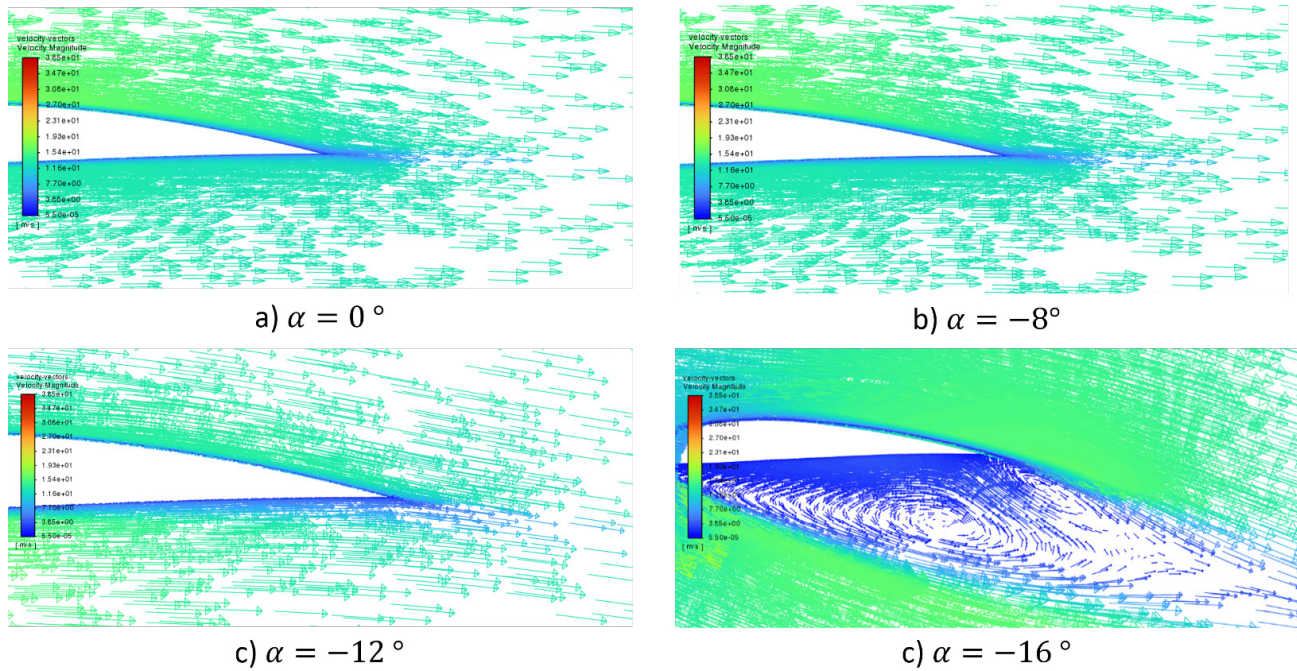


Figure 10 : Influence of a negative angle of attack on the location of stagnation point and the velocity distribution around the airfoil trailing edge

In conclusion, results obtained from CFD calculations of incompressible flow around the cambered airfoil at zero, positive and negative angle of attack indicate the flow conditions around the airfoil leading edge, the flow separation along the airfoil top and bottom surface and the vortices formation behind the airfoil trailing edge.

### 2.3.1.3 Flow field adaptation in front of and behind the airfoil

Velocity profiles are shown along the flow domain at the following locations: inlet, line 1 at 100mm in front of the airfoil, line 2 at 10mm in front of the airfoil, line 5 at 10mm behind the airfoil, line 6 at 50mm behind the airfoil, line 7 at 100mm behind the airfoil, line 8 at 200mm behind the airfoil and at outlet.

Velocity profiles at zero angle of attack in front of and behind the airfoil are shown in Figure 11. The velocity at the inlet is constant as assigned, while the velocity profile is disturbed moving closer in front of the airfoil (Figure 11a) and behind the airfoil (Figure 11b).

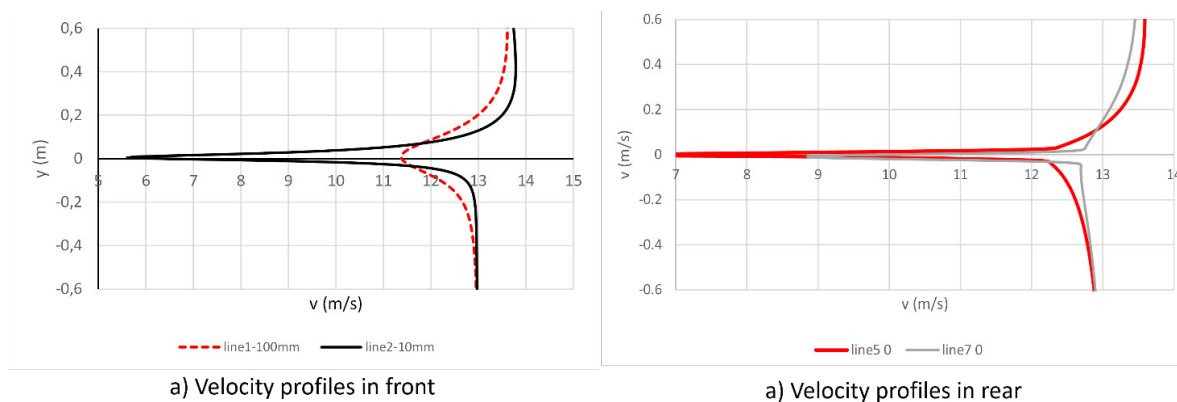


Figure 11 : Comparison of velocity profiles in front and in rear of the airfoil for angle of attack :

In front of the airfoil, the intensity of velocity profile change is higher closer to the airfoil and more stable further away from the airfoil. The symmetrical velocity profile in front of the airfoil indicates there is a shock-free flow. Behind the airfoil, the velocity profile is disturbed due to the airfoil presence, while flow uniformity is achieved further away from the airfoil.

In case of positive and negative angle of attack, velocity profiles in front of the airfoil are given in Figure 12. Figure 12 left shows the velocity profile at 100mm in front of the airfoil; it can be seen that the velocity profile is more uniform by height (changing between 13-14m/s) at  $0^\circ$  except in the area affected by the airfoil presence ( $y=\pm 0,2\text{m}$ ) with velocity of 11,5m/s, whereas for positive angle of attack  $+8^\circ$  there is an acceleration above the top surface ( $\sim 15\text{ m/s}$ ) since it is a low pressure zone and deceleration below the bottom surface ( $\sim 12\text{ m/s}$ ) since it is a high pressure zone; for negative angle of attack  $-8^\circ$  the deceleration is above the top surface ( $\sim 11\text{ m/s}$ ) and the acceleration is below the bottom surface ( $\sim 14.5\text{ m/s}$ ).

Figure 12 right shows the velocity profile at 10mm in front of the airfoil; the velocity profile is more uniform by height (between 13-14m/s) at  $0^\circ$  except in the area affected by the airfoil presence ( $y=\pm 0,2\text{m}$ ) when the velocity lowers to 5.5m/s. For positive angle of attack  $+8^\circ$  there is a more noticeable acceleration above the top surface ( $\sim 17.5\text{ m/s}$ ) and deceleration below the bottom surface ( $\sim 7\text{ m/s}$ ). For negative angle of attack of  $-8^\circ$  the deceleration is above the top surface ( $\sim 6.5\text{ m/s}$ ) and the acceleration is below the bottom surface ( $\sim 19.2\text{ m/s}$ ).

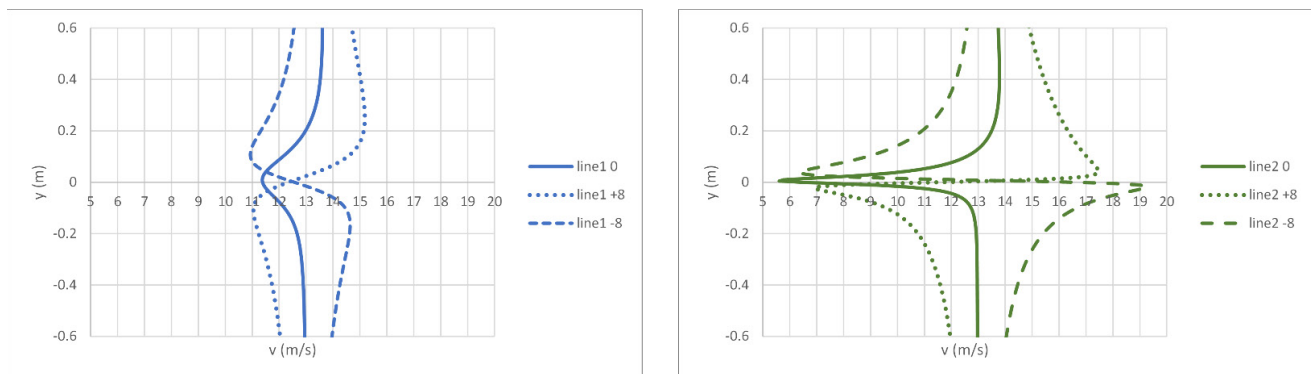


Figure 12 : Comparison of velocity profiles for angles of attack:  $0^\circ$ ,  $+8^\circ$  and  $-8^\circ$  at 100mm in front of the airfoil (left) and 10mm in front of the airfoil (right)

The results show that velocity is higher at the airfoil top surface in case of positive angle of attack and higher at the airfoil bottom surface in case of negative angle of attack.

In case of positive and negative angle of attack, velocity profiles behind the airfoil are given in Figure 13. Figure 13 left shows the velocity profile at 10mm behind the airfoil; it can be seen that the velocity profile is more uniform by height for all angles of attack except in the area affected by the airfoil trailing edge ( $y=\pm 0,05\text{m}$ ) when the velocity abruptly decreases (from  $\sim 12.5\text{m/s}$  to  $6\text{m/s}$  for  $0^\circ$  and  $-8^\circ$ ) especially for  $-8^\circ$  for which the airfoil bottom surface characterizes with air flow deceleration (from  $\sim 12.5\text{m/s}$  to  $4/5\text{m/s}$ ). The velocity changes are smaller at 200mm behind the airfoil as shown in Figure 9 right, i.e., from  $\sim 13\text{m/s}$  to  $10\div 10.5\text{m/s}$ .



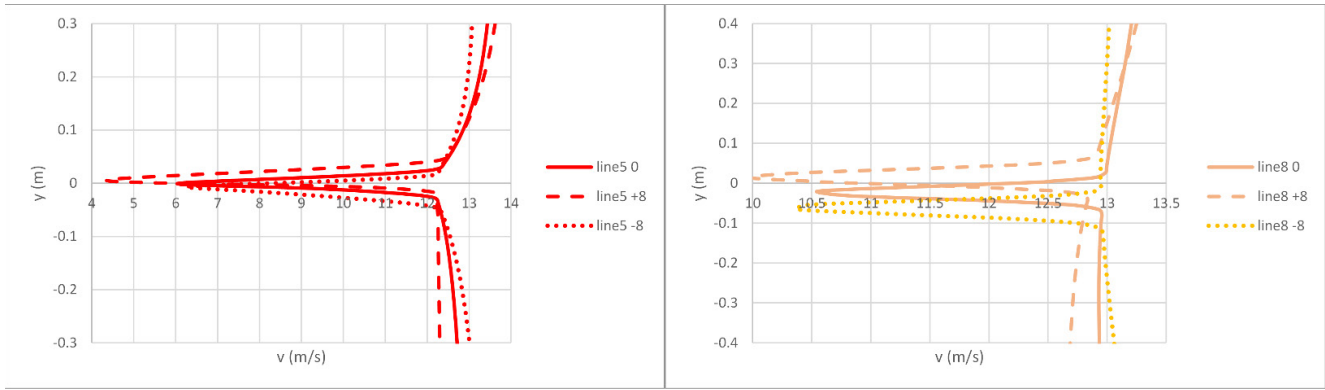


Figure 13 : Comparison of velocity profiles for angles of attack:  $0^\circ$ ,  $+8^\circ$  and  $-8^\circ$  at 10mm behind the airfoil (left) and 200mm behind the airfoil (right)

Higher disturbance of velocity profile behind the NACA 4412 airfoil is caused in case of a negative angle of attack.

### 2.3.2 Pressure distribution

The relation between pressure and velocity in a flow is represented by the Bernoulli equation which states that total pressure  $p_{tot}$  is constant along a streamline in a fluid flow. Total pressure is the sum of static pressure  $p$  and dynamic pressure  $p_{dyn}$ , i.e.:

$$p_{tot} = p + p_{dyn} = p + \rho \frac{v^2}{2}$$

Dynamic pressure can be measured (as difference between total and static pressure) in flight by using a Pitot-tube to determine the aircraft speed :

$$v = \sqrt{\frac{2p_{dyn}}{\rho}} = \sqrt{\frac{2(p_{tot} - p)}{\rho}}$$

According to the vectors of velocity distribution, at zero angle of attack, the upper surface of the airfoil has higher dynamic pressure due to the higher velocity, while the bottom surface has lower dynamic pressure. By increasing the angle of attack, the dynamic pressure further decreases at the bottom surface because of air deceleration.

At zero angle of attack, static pressure at the bottom surface is higher than at the upper surface. Increasing the angle of attack leads to higher static pressure at the bottom surface. For higher positive angles of attack, in the areas of flow separation on the upper surface close to the trailing edge, the velocity decreases causing increase of static pressure; the static pressure is low on the upper surface close to the leading edge where the velocity is highest.

The pressure coefficient  $C_p$  describes the relative pressure in the flow field as a ratio between the static and dynamic pressure, i.e.:

$$c_p = \frac{p - p_\infty}{\frac{1}{2} \rho_\infty v_\infty^2}$$

where  $p_\infty, v_\infty$  is the static pressure and velocity of the freestream and  $\rho$  is the freestream fluid density.

Figure 14 shows pressure coefficient distribution along the airfoil at angles of attack  $0^\circ$ ,  $+8^\circ$  and  $-8^\circ$ . For zero angle of attack, the stagnation point is at the airfoil leading edge where velocity is zero and the static pressure is highest thus  $C_p$  is highest at this location. Since the fluid accelerates on the upper surface, the static pressure is higher, and the dynamic pressure is lower on the bottom surface where the  $C_p$  has higher absolute values compared to the upper surface.

By increasing the positive angle of attack, the static pressure on the bottom surface is getting higher, while the dynamic pressure is lower because of the deceleration so the values of  $C_p$  are higher along the bottom surface; on the other hand, there are negative values of  $C_p$  at the upper surface since the dynamic pressure is higher than the static pressure i.e., the fluid accelerates at the upper surface for positive angles of attack.

For negative angles of attack, the static pressure is higher on the upper surface, for which  $C_p$  values are higher compared to bottom surface. Increasing the negative angle of attack leads to higher negative values of  $C_p$  on the bottom surface.

As much as the angle of attack is higher, the pressure difference between the upper and bottom surface of the airfoil increases which means generation of a higher lift. It can be concluded that most of the lift is generated at the front part of the airfoil, closer to the leading edge.

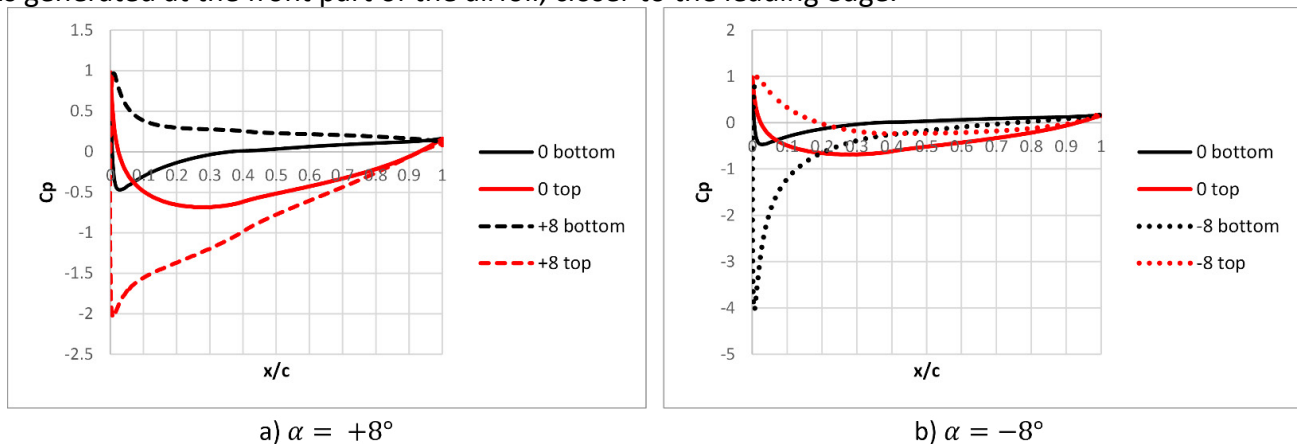


Figure 14 : Comparison of pressure coefficient in relation to attack angle  $00$  for different angles of attack: a)  $+8^\circ$ ; b)  $-8^\circ$

At zero angle of attack, negative value of pressure coefficient on the top surface is obtained. In case of positive angle of attack, the value of pressure coefficient on the airfoil top surface is negative and with higher magnitude compared to zero angle of attack. For a negative angle of attack, the value of pressure coefficient on top surface is positive and larger than in the case of zero angle of attack.

### 2.3.3 Aerodynamic characteristics

The airfoil characteristic is indicated by the values of the lift coefficient and drag coefficient for an angle of attack  $\alpha$ . They are aerodynamic parameters which influence performance.



### 2.3.3.1 lift coefficient $C_l$

The lift coefficient is calculated as:

$$C_L = \frac{L}{\frac{1}{2} \rho v^2 A}$$

The lift coefficient value is obtained directly from Ansys Fluent. The change of the lift coefficient for different angles of attack is shown in Figure 15 for both the experimental [7] and numerical case. It can be seen that good agreement with experimental data is achieved for range of angles from  $-8^\circ$  to  $+8^\circ$ ; out of this region, higher discrepancies are present, but the trend of the lift curve is the same.

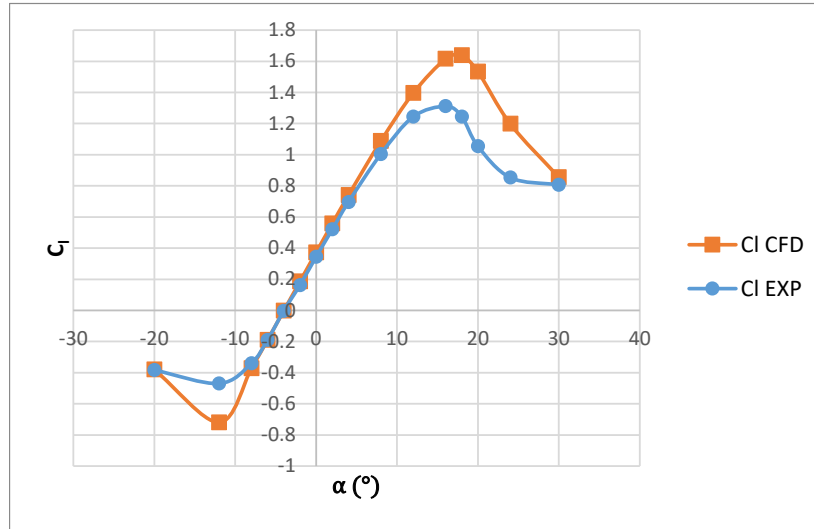


Figure 15 : Lift Coefficient dependence on angle of attack

By increasing the angle of attack in positive or negative direction, the lift force increases and depending on the angle of attack, it can be directed vertically upwards (positive lift) or downwards (negative lift). The lift coefficient is positive for angle of attack in the range  $-4^\circ$  to  $20^\circ$  and it is negative for angle of attack in the range  $-20$  to  $-4^\circ$ .

In this case, the lift force is zero at negative angle of attack, i.e.  $\sim -4^\circ$  (also called the zero-lift angle of attack) because the airfoil analyzed is with a positive camber (above the chord line). It can be noted that at low to moderate angles of attack, the lift coefficient varies linearly with the angle of attack; for this range of angles of attack the air flows smoothly over the surface and is attached on most part of the airfoil as shown in Figure 7a, b, c and Figure 9b.

As the angle of attack increases, the lift coefficient also increases until reaching a maximum value prior to a certain angle of attack called the stall angle when the flow is separated (Figure 8c). Beyond this angle (Figure 8d), the aircraft shouldn't operate due to stability issues and difficulties with control. According to the results, maximum lift coefficient of  $C_{l_{\max}} = 1.64$  is achieved at stall angle  $18^\circ$  (which actually corresponds to angle of  $16^\circ$  in the experiment). Further increment of the angle of attack above the stall angle value causes a significant decrease in lift coefficient due to large increase in drag and the curve  $cl$  is not linear furthermore.

The results from CFD calculations give higher value of  $Cl$  for both positive and negative angles of attack which alludes to the need of incorporating additional input data such as surface roughness, variable thermophysical properties of fluid etc.

### 2.3.3.2 drag coefficient $C_d$

The drag coefficient is calculated as:

The drag coefficient value is obtained directly from Ansys Fluent. The change of the drag coefficient for different angles of attack is shown in Figure 16 for both the experimental and numerical case. It can be seen that good agreement with experimental data is achieved for range of angles from  $-8^\circ$  to  $+16^\circ$ ; out of this region, higher discrepancies are present.

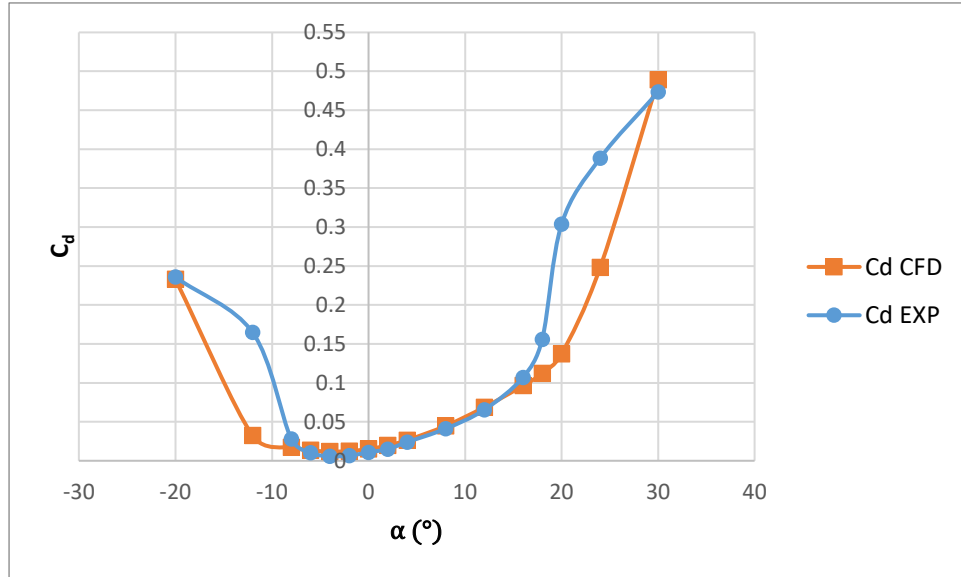


Figure 16 : Drag Coefficient dependence on angle of attack

The drag force can only be positive – acting opposite of the solid body motion, so the drag coefficient is always positive and it increases with increasing the absolute value of the angle of attack. At higher angles of attack, the drag coefficient is higher because flow separation occurs close to the trailing edge and vortices are formed around the trailing edge contributing to the drag force. The drag coefficient physically originates from the viscous effects of skin friction (skin friction drag) and flow separation (pressure drag).

### 3. Conclusions

Ansys Workbench is used as a tool to model and simulate turbulent flow around airfoil NACA4412 in an infinite freestream. The whole process of geometry creation, meshing, solving and data processing is performed in Ansys Workbench which integrates all steps. Numerically obtained results are compared with available experimental data. Results on velocity and pressure distribution and airfoil aerodynamic characteristics are discussed. The analysis shows the influence of the airfoil presence on the flow field i.e., the destabilization and non-uniformity of the velocity distribution close to the airfoil body. It is seen that the airfoil position in the flow field represented by the angle of attack affects the fluid adaptation to the solid body.

## 4. References

- [1] Y. B. R. F. Nakayama, Introduction to Fluid Mechanics, Butterworth-Heinemann, 1999.
- J. John D. Anderson, Fundamentals of Aerodynamics, McGRAW-HILL, 2017.
- [2] F. M. M. H. D. W. M. G. S. Stern, "Measurement of pressure distribution and forces acting on an airfoil," University of Iowa, Iowa, 2004.
- [3] R. F., Aerofoil sections-Results from wind-tunnel investigations, theoretical foundations, London: Butterworths, 1961.
- [4] C. W. J. H. A. S. a. S. D. W. Ladson C. L., "Computer program to obtain ordinates for NACA airfoils," NASA Technical Memorandum 4741, 1996.
- [5] "NACA 4 digit airfoil generator," [Online]. Available: <http://airfoiltools.com/airfoil/>
- [6] R. M. Pinkerton, "THE VARIATION WITH REYNOLDS NUMBER OF PRESSURE DISTRIBUTION OVER AN AIRFOIL SECTION," NACA, Washington, 1936.
- [7] F. T. J. a. P. R. S. Steven R. Allmaras, "Modifications and Clarifications for the Implementation of the Spalart-Allmaras Turbulence Model," in *Seventh International Conference on Computational Fluid Dynamics (ICCFD7)*, Big Island, Hawaii, 2012.

© 2024 ANSYS, Inc. All rights reserved.

## Use and Reproduction

The content used in this resource may only be used or reproduced for teaching purposes; and any commercial use is strictly prohibited.

## Document Information

This case study is part of a set of teaching resources to help introduce students to topics focused on fluid dynamics and related topics.

## Ansys Education Resources

To access more undergraduate education resources, including lecture presentations with notes, exercises with worked solutions, MicroProjects, real life examples and more, visit [www.ansys.com/education-resources](http://www.ansys.com/education-resources).

## Feedback

If you notice any errors in this resource or need to get in contact with the authors, please email us at [education@ansys.com](mailto:education@ansys.com).

**ANSYS, Inc.**  
Southpointe  
2600 Ansys Drive  
Canonsburg, PA 15317  
U.S.A.  
724.746.3304  
[ansysinfo@ansys.com](mailto:ansysinfo@ansys.com)

If you've ever seen a rocket launch, flown on an airplane, driven a car, used a computer, touched a mobile device, crossed a bridge or put on wearable technology, chances are you've used a product where Ansys software played a critical role in its creation. Ansys is the global leader in engineering simulation. We help the world's most innovative companies deliver radically better products to their customers. By offering the best and broadest portfolio of engineering simulation software, we help them solve the most complex design challenges and engineer products limited only by imagination.

visit [www.ansys.com](http://www.ansys.com) for more information

Any and all ANSYS, Inc. brand, product, service and feature names, logos and slogans are registered trademarks or trademarks of ANSYS, Inc. or its subsidiaries in the United States or other countries. All other brand, product, service and feature names or trademarks are the property of their respective owners.

© 2024 ANSYS, Inc. All Rights Reserved.